Three Brain SPECT Region-of-Interest Templates in Elderly People: Normative Values, Hemispheric Asymmetries, and a Comparison of Single- and Multihead Cameras

Nancy J. Lobaugh, Curtis B. Caldwell, Sandra E. Black, Farrell S. Leibovitch, and Richard H. Swartz

Rotman Research Institute, Baycrest Centre for Geriatric Care, Toronto; Cognitive Neurology Unit and Research Program in Aging and Department of Medical Imaging, Sunnybrook and Women's College Health Sciences Centre, Toronto; and Departments of Medicine and Medical Imaging and Institute of Medical Science, University of Toronto, Toronto, Canada

The purpose of this study was to generate anatomically guided region-of-interest (ROI) brain SPECT templates based on scans of elderly healthy volunteers. We describe normal tracer uptake and hemispheric asymmetries for each of 3 camera systems and compare these characteristics among systems. **Methods:** ^{99m}Tc-hexamethyl propyleneamine oxime SPECT scans were acquired from 28 elderly healthy volunteers (mean age [±SD], 70.3 ± 6.5 y) on a single-head rotating γ camera (n = 15) or on dual- (n = 18) or triple-head (n = 13) cameras. The average number of counts in each ROI was calculated and referenced to counts in a cerebellar ROI, providing semiquantitative regional cerebral blood flow (rCBF) ratios. For the templates and ROI map, base images of a healthy volunteer were obtained with each camera. Data from individuals scanned with 2 cameras on the same day (n = 15) were used to evaluate rCBF differences across cameras. For each camera, averaged SPECT templates were made using automated image registration. The base volunteer's T1-weighted MR image was converted to stereotactic space with dimensions similar to those of the SPECT templates, and 79 bilateral ROIs were defined. To obtain ROI rCBF ratios, we aligned individual images to their appropriate template and then to this modified MR image. **Results:** The ROI coefficients of variation indicated that the fit of the ROIs was acceptable (0.07–0.35). Mean rCBF ratios ranged from 0.57 to 1.0, 0.67 to 1.01, and 0.63 to 1.00 for single-, dual-, and triple-head cameras, respectively. The cuneus, occipital cortex, occipital pole, middle temporal gyrus, and posterior middle frontal gyrus showed consistent hemispheric asymmetry (right side greater than left side in 83%–100% of individuals). Mean rCBF ratios did not differ between dual- and triple-head cameras, whereas the ratios for single- and dual-head cameras differed significantly (39 ROIs differed), even after smoothing and filtering the dual-head images to the level of the single-head images. **Conclusion:** The use of SPECT templates based on elderly healthy volunteers is an important feature of this technique because most available templates have used young individuals. Another important feature is the use of MR image–based ROIs. These procedures are versatile because they use more than 1 camera. They can easily be implemented in clinical and research settings to detect camera-specific, abnormal deviations in rCBF ROI ratios and asymmetry magnitudes in diseases associated with aging, such as stroke and dementia.

Key Words: ^{99m}Tc–hexamethyl propyleneamine oxime brain SPECT templates; regions of interest; aging; image registration; hemispheric asymmetries

J Nucl Med 2000; 41:45–56

SPECT with ^{99m}Tc-hexamethyl propyleneamine oxime (HMPAO) is widely used for diagnosing deficits in regional cerebral blood flow (rCBF) in several neurologic diseases, including stroke and dementia, that affect elderly people. In the SPECT method, absolute rCBF values are not obtained. However, tracer uptake values referenced to tracer uptake in a standard region reflect an estimate of relative rCBF values. The highest degree of anatomic precision for accurately describing the location and magnitude of flow changes is obtained by acquiring both structural MR images and functional SPECT images for each patient (*1*). Regions of interest (ROIs) are drawn for each patient on the structural image. The ROIs are then applied to the functional image, which has been coregistered to the MR image (*2–4*). However, this method is laborious and costly and may not be feasible in large populations. To address this drawback, we adopted an approach in which SPECT images are first standardized into a common space, which has the advantage of facilitating intersubject comparisons (*5*). This common space was defined by creating 3 HMPAO SPECT templates (for single-, dual-, and triple-head γ cameras) using images from, respectively, 15, 18, and 13 elderly healthy volunteers. Anatomic specificity was obtained using a set of 79 ROIs that were defined on the structural MR image from 1 healthy volunteer who underwent brain SPECT with all 3 cameras. The ROIs were drawn separately for the 2 hemispheres and thus reflect inherent hemispheric asymmetry in

Received Nov. 12, 1998; revision accepted Jun. 21, 1999.

For correspondence or reprints contact: Nancy J. Lobaugh, PhD, Imaging/Bioengineering Research, Rm. S604, Sunnybrook and Women's College Health Sciences Centre, 2075 Bayview Ave., Toronto, Ontario M4N 3M5, Canada.

volume and location of cortical regions. Using elderly rather than young individuals as the basis for the templates accounts for the mean flow changes frequently seen with normal aging (*6–9*). The methods used to generate the templates and ROI maps, followed by semiquantitative rCBF results for the 3 cameras, are presented.

In brain SPECT, as in other nuclear medicine procedures, one must maintain a balance between achieving high sensitivity (number of photons detected) and accurately resolving the radionuclide distribution in the body. The sensitivity and resolution are determined by the conjoint characteristics of the collimator used, the dose injected, and the length of the study. Because the injected dose for brain SPECT is normally standardized at any given institution and most patients sent for brain SPECT studies cannot remain still for more than 20–30 min, the choice of collimator becomes the primary factor. The entry of dual- and triple-head γ cameras into the field has improved the sensitivity of γ camera systems. This improvement has allowed the use of novel high-resolution collimators, such as the fanbeam type, which improve sensitivity while retaining resolution equivalent to that of conventional parallel-hole collimators. In addition, some multihead cameras provide increased spatial resolution through decreased brain reach (i.e., reduced distance from the edge of the camera to the imaging field of view, allowing the camera to image closer to the patient).

Analysis of the impact of camera differences has been restricted to issues of sensitivity and spatial resolution (*10,11*) or has focused on collimator differences (*12*). However, to our knowledge, no one has directly compared rCBF ratios obtained with different cameras, although similarity in rCBF ratios is an implicit assumption. This assumption becomes critical in large-scale studies in which multiple cameras may be in use and data are pooled across cameras. The assumption also has direct implications in clinical settings, because the normal range of rCBF values may vary between cameras. Because of this uncertainty, separate templates were constructed for each camera. Several of our healthy volunteers were scanned with 2 cameras on the same day (single and dual or dual and triple), permitting direct comparison of rCBF ratio differences between each pair of cameras.

MATERIALS AND METHODS

Healthy Volunteers

Healthy volunteers with acceptable scans (14 women, 14 men; age range, 56.6–81.4 y; mean age [±SD], 70.3 ± 6.5 y) were selected from our control database. Exclusion criteria for the scans were incomplete visualization of cerebella (3 individuals) or sinuses with high activity that could not be distinguished from brain activity or caused alignment errors (4 individuals). Fifteen individuals were scanned with 2 cameras on the same day and thus contribute to 2 templates. Seven of these 15 contributed to both the single- and dual-head templates. The remaining 8 contributed to the dual- and triple-head templates. Three individuals were scanned with all 3 cameras (single and dual on the first visit, dual and triple on a follow-up visit). In these instances, images from the first visit (single and dual) were used only for the templates, and images from the second visit (dual and triple) were used only for camera comparisons. Table 1 shows the distribution of healthy volunteers across cameras, along with age and handedness for each group. All healthy volunteers had normal cognitive function as assessed by an extensive neuropsychologic battery that included tests of general function, language, praxis, visuospatial abilities, memory, executive function, and nonverbal abilities. In addition, no individual had a history of stroke or other neurologic abnormalities at the time of scanning, and an experienced nuclear medicine physician judged all SPECT images to show normal findings.

SPECT Images for Templates

^{99m}Tc-HMPAO was prepared using the methods described in the package insert for the Ceretec kit (Medi-Physics, Inc., Amersham Healthcare, Arlington Heights, IL). Radiopharmaceutical was not injected unless the fraction of bound ^{99m}Tc exceeded 90%. Typically, this fraction exceeded 97%. In all instances, the radiopharmaceutical was injected within 30 min of reconstitution. SPECT was initiated a minimum of 15 min and a maximum of 2 h after intravenous injection.

Single-head SPECT images were acquired between 1992 and 1996 with a 400AT γ camera (General Electric Medical Systems, Milwaukee, WI) fitted with low-energy, high-resolution, parallel-hole collimators. A 64 × 64 pixel acquisition matrix with an acquisition zoom of 1.33 was used, and 64 frames were acquired over 360° in step-and-shoot mode. Each frame was acquired for 25 s. Total acquisition time (including the time to move between steps)

TABLE 1
Healthy Volunteers Contributing to Normal ROIs and Camera Comparisons

	Participants				Cameras		
Camera	Men (n)	Women (n)	Handedness (n)	Age (y) (mean [±SD])	Single–dual	Dual–triple	Not used*
Single-head	7	8	14 R, 1 L	71.9 (5.1)	7	—	8
Dual-head	8	10	16 R, 1 L, 1 B	71.0 (7.5)	7	8	3
Triple-head	6	7	11 R, 1 L, 1 B	68.5 (7.7)	—	8	5†
Total	14	14	24 R, 2 L, 1 B	70.3 (6.5)			

*Individuals scanned with only 1 camera.
†Follow-up dual–triple scans were available for 3 individuals and were used for only dual–triple comparison to increase sample size to 11.
B = ambidextrous.

was approximately 30 min. The raw data from the single-head camera were reconstructed using filtered backprojection. A Butterworth filter with a cutoff of 0.35/cm and a power factor of 10 was used. A correction that assumed uniform photon attenuation throughout the head was applied. Data were corrected for backdiffusion using the cerebellum as the reference region (*13,14*). Voxel sizes in the final images were 4.8 × 4.8 × 9.6 mm, and images contained 18–24 slices.

Dual-head SPECT images were acquired between 1993 and 1997 with a 2000 γ camera (Picker International, Inc., Cleveland, OH) fitted with ultra-high-resolution fanbeam collimators. A 128 × 128 pixel acquisition matrix was used with an acquisition zoom of 1.0, and 120 frames were acquired over 360° (i.e., 60 frames per camera head) in continuous-acquisition mode. Each frame was acquired for 20 s. The total acquisition time was 20 min.

Triple-head SPECT images were acquired in 1997 and 1998 with a 3000 XP γ camera (Picker International) fitted with ultra-high-resolution fanbeam collimators. A 128 × 128 pixel acquisition matrix was used with an acquisition zoom of 1.0, and 120 frames were acquired over 360° (i.e., 40 frames per camera head) in continuous-acquisition mode. Each frame was acquired for 28 s. The total acquisition time was 18.7 min. The time per frame varied somewhat for the dual- and triple-head scans. If an individual could not stay still for the total acquisition time, the scan was repeated with shorter times per frame.

To reconstruct the dual- and triple-head images, ramp-filtered backprojection was used, followed by a 3-dimensional postfilter (Wiener filter, default 1.0). This reconstruction was followed by attenuation correction using the first-order method of Chang (*15*). Voxel sizes were 2.17 × 2.17 × 4.67 mm and 2.17 × 2.17 × 3.56 mm in the dual- and triple-head images, respectively. The number of slices ranged from 33 to 49 in the dual- and 37 to 57 in the triple-head images.

The reconstructed images were visually inspected, and if regions outside the brain had activity higher than that in the brain, the pixel values in these regions were set to the maximum count in the brain (usually cerebellum). This procedure minimized the variations in rCBF ratios noted by Loutfi and Singh (*16*), caused by variability in cerebellar counts in stroke and head injury. After reconstruction the images were transferred to a SPARC workstation (Sun Microsystems, Inc, Mountain View, CA) and converted to 8-bit ANALYZE format (Biomedical Imaging Resource, Mayo Foundation, Rochester, MN) for further processing. The pixel values in areas of high activity outside the brain (e.g., sinuses, salivary glands, and parotid glands) were set to 0 when they interfered with the alignment procedures. However, because high activity is frequently seen in these regions, these pixel values were left in for most images.

Selection of Base Image for the Templates

Four of the healthy volunteers (2 women, 2 men) in our database had undergone SPECT with all 3 cameras and MRI within 4 months of base SPECT. These individuals' images were examined for their suitability as the base SPECT image for the templates as well as for the MR image–based ROI map. One was excluded because abnormalities were noted on the most recent scan, which preceded a subsequent stroke. Two were excluded because the presence of sulcal enlargement did not permit the adequate removal of skull and meninges from the brain on the MR image, which was required for aligning the template and drawing the ROI map. The individual selected was a 73.5-y-old woman for whom all 3 cameras showed complete brain perfusion and for whom skull and meninges were successfully removed from the MR image. Single- and dual-head SPECT images were selected from her first visit, and the triple-head SPECT image was from her follow-up visit, 1 y 7 mo later. No atrophy or other abnormalities were noted on her follow-up MR image (2 d before acquiring the triple-head SPECT images), so her base MR image was used for placement of the ROIs. The T1-weighted MR image used to define the ROIs was acquired with a Signa scanner (General Electric Medical Systems) 4 months after the base single- and dual-head SPECT images were acquired. The MRI parameters were 1.5 T, a 3-dimensional axial volume, spoiled gradient-refocused acquisition in the steady state, a 35° flip angle, an echo time of 5, a repetition time of 24, a 22-cm field of view, a 1.22-mm slice thickness, 124 images, a 192 × 256 matrix, 1 excitation, and 7.26 min of total scanning time.

SPECT–SPECT Registration and Templates

The SPECT templates were created using the version 3.07 automated image registration (AIR) package of Woods et al. (*17,18*), which a study recently showed to provide adequate alignment of SPECT images (*19*). In that study, maximum anatomic variability was 4.7 mm, measured as location error when the transformations were applied to x-ray CT scans. The Appendix provides details of the alignment parameters. Briefly, a 12-parameter affine model using a least-squares-with-intensity-scaling cost function was used to coregister all SPECT images to the base SPECT image. A common space was then defined for the images, and they were averaged to form the SPECT templates. The single-head template was 64 × 64 × 18 voxels, the dual-head template was 128 × 128 × 38 voxels, and the triple-head template was 128 × 128 × 45 voxels.

MRI–SPECT Coregistration

The base T1-weighted MR image was manually rotated such that the line passing through the anterior and posterior commissures was in the horizontal plane, generally referred to as stereotactic space (*20*). The final image size was 256 × 256 × 145 voxels, with each voxel measuring 0.859 mm^3. The skull and meninges were removed from the image using the erosion procedure in iMIPS software (Integrated Medical Imaging Processing Systems, Inc., Pembroke, MA). The eroded MR image was then resliced, using AIR, into a space similar to the dimensions of the SPECT templates. The resliced MR image was 128 × 128 × 50 voxels (voxel dimensions, 1.72 × 1.72 × 2.67 mm). This image size maintained sufficient anatomic detail for drawing the ROI map while minimizing the size of transforms for the SPECT images. Transformation matrices to align SPECT images and SPECT templates to the resliced MR image were generated using a 6-parameter rigid-body model, maintaining the voxel anisotropy of the resliced MR image.

ROI Maps

Two ROI maps, 1 for each hemisphere, were generated using version 1.1 ANALYZE AVW (Biomedical Imaging Resource) and saved as ANALYZE object files. These maps were based in part on the nomenclature and demarcations of Damasio (*21*) and Talairach and Tournoux (*20*). The eroded, resliced MR image was divided into volumes containing the left and right hemisphere. ROIs on the lateral and medial cortical surfaces were identified on the basis of sulcal landmarks, and the surfaces were color coded. The MR image was then displayed in the axial plane, and the cortical ROIs

were drawn using the surface markings as guidelines. ROIs for subcortical structures, cerebrospinal fluid, and major white-matter tracts were also drawn at that time. The cerebrospinal fluid and white-matter ROIs covered multiple levels within the brain. Being quite large, these ROIs did not accurately reflect regional perfusion in these areas. For all other ROIs, care was taken to ensure that the volume of each was within the resolution of the single-head camera. The smallest ROIs were in the medial temporal lobe and encompassed approximately 2 cm^3, or the equivalent of approximately 10, 100, and 130 voxels with the single-, dual-, and triple-head cameras, respectively.

To provide normative values and examine the adequacy of the ROI map, all control images were aligned to the templates using the 12-parameter affine model of AIR and then resliced into MR image space. For each ROI, the mean, SD, maximum and minimum counts, locations (on x-, y-, and z-axes) of the maximum and minimum counts, and number of voxels were calculated using a program written in C++. This procedure combined all slices in an ROI into a single object, thus producing an ROI volume. The ROI mean counts were transformed to provide semiquantitative rCBF ratios by dividing the mean counts for each ROI by the mean cerebellar counts.

The first step in assessing the ROI map involved aligning the templates to the base MR image. The ROIs were superimposed slice-by-slice on each of the 3 SPECT templates and visually inspected. The coefficient of variation (SD/mean counts) provided a quantitative metric of the goodness of the fit. High coefficients of variation were associated with ROIs that extended beyond template activity. When the coefficients were high, the ROI was edited to ensure that it was placed over the signal in each template. The ROI map was then further assessed by superimposing it on the individual SPECT images. Because the cerebellum is frequently used to normalize SPECT counts (*22,23*), the cerebellar ROI was further edited so that it never extended beyond regions of cerebellar activity in the healthy volunteers. Several healthy volunteers had no data in the bottom 4 slices of the cerebellum as seen on the MR image, and these slices were not included in the cerebellar ROI. The next 3 slices of the cerebellum (bilaterally) were treated as separate ROIs, because these slices frequently do not contain data after the images are aligned to the baseline MR image. If the coefficient of variation in these slices was low in the aligned images, the counts were automatically incorporated into the larger cerebellar ROI. (We used a threshold coefficient of variation of 0.32 to determine whether to include these slices. This is the average of the 2-SD values for the coefficient of variation in the 3 cameras.) To date, we have found only 3 of more than 200 aligned scans that do not have data in the remaining slices containing the cerebellar ROI. Table 2 presents regions included in the ROI map, with Brodmann's area (BA) and ROI volume.

TABLE 2
ROI Locations, BAs, and Volumes

ROI	BA	ROI volume (cm^3) Right	Left
Cortical medial surface			
Paracentral lobule	4/5	5.83	4.73
Precuneus	7	13.97	13.52
Cuneus	17/18/19	10.40	8.87
Lingual gyrus	18/19	6.07	7.50
Retrosplenial cortex	26/29/30	3.38	2.54
Cingulate cortex: 5 ROIs			
Cingulate1	25	3.60	3.33
Cingulate2	24/32/33	4.56	3.42
Cingulate3	24/32/33	4.13	4.90
Cingulate4	23/31	4.43	4.03
Cingulate5	23/31	4.14	4.12
Cortical lateral surface			
Frontal pole	10	13.18	11.32
Orbital frontal gyrus	11	11.73	14.37
Inferior frontal gyrus, posterior	44	8.88	8.70
Inferior frontal gyrus, anterior	45	6.91	7.20
Middle frontal gyrus, posterior	8/9	13.45	13.69
Middle frontal gyrus, anterior	46	12.24	8.54
Superior frontal gyrus, posterior	6/8	15.61	15.78
Superior frontal gyrus, anterior	8/9	13.92	13.72
Precentral gyrus	4	21.43	23.72
Postcentral gyrus	5/1/2/3	15.40	21.05
Superior parietal lobe	7	16.78	14.01
Supramarginal gyrus	40	10.19	10.57
Angular gyrus	39	9.94	8.48
Occipital cortex	18/19	31.32	32.73
Occipital pole	17	5.43	5.60
Temporal lobe			
Temporal pole	38	9.84	10.36
Inferior temporal gyrus	20/37	16.47	17.68
Inferior temporal, medial (fusiform gyrus, parahippocampal gyrus)	28/35/36/37	11.87	8.80
Middle temporal gyrus	21/37	15.44	14.86
Middle temporal, medial (parahippocampal gyrus, perirhinal cortex, amygdala)	28/35/36	13.58	13.46
Superior temporal gyrus	22/41/42	11.59	17.29
Superior temporal, medial (entorhinal cortex, subiculum)	27/34	2.25	1.90
Hippocampal area	35	2.71	2.49
Other			
Insula		15.53	12.65
Caudate/putamen		12.24	13.06
Thalamus/hypothalamus		10.73	10.75
Pons		18.02	
Cerebellum		40.86	41.62
White matter		90.53	99.09
Cerebrospinal fluid		16.71	15.20

RESULTS

General Findings

Figure 1 shows the placement of the ROIs, with the left ROIs overlying selected axial slices of the MR image. Table 3 presents means and ranges for the ROI rCBF ratios (cerebellar reference) and coefficients of variation across ROIs (normative values for individual ROIs are available from us). The rCBF ratios in cerebrospinal fluid and white matter were low, as expected, for all cameras (0.58 and 0.71, respectively, for single-head cameras; 0.45 and 0.64, respectively, for dual-head cameras; 0.43 and 0.64, respectively, for triple-head cameras).

The fit of the ROI map to images aligned to each template was good as assessed by examining the ROI coefficients of variation. In the single-head images, only 3 regions had coefficients of variation greater than 2 SDs above the mean

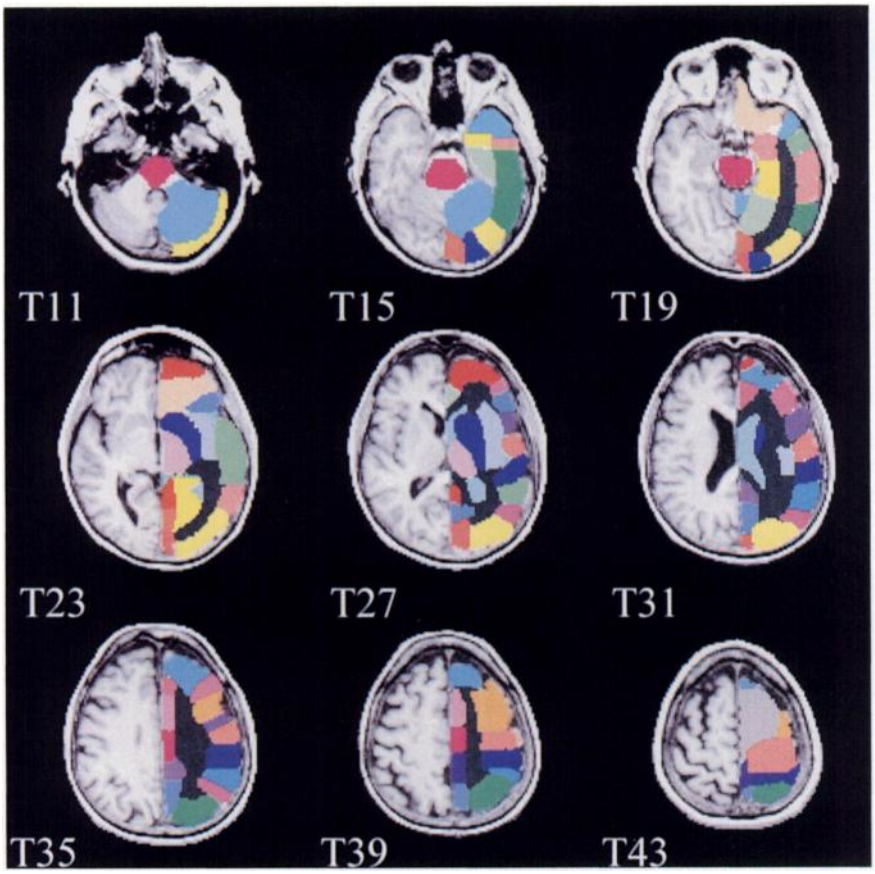

FIGURE 1. Representative axial slices through base MR image, with left ROI map superimposed. ROIs for right hemisphere were drawn separately and are similar to those for left hemisphere. Brain tissue is visible on slices 3–49 in modified MR image, and ROIs have been placed on slices 6–47. At lower left of each slice is slice number (2.66-mm slice thickness). Leftmost slices in each row, from top to bottom, roughly correspond to the following in Talairach and Tournoux (*20*): 11–12a (−28 mm); 8–9a (+1 mm); 5–6 (+28 mm).

coefficient of variation for all ROIs. These regions were the left cuneus, left occipital pole, and left lingual gyrus, which had coefficients of variation (±SD) of 0.32 (±0.04), 0.31 (±0.03), and 0.30 (±0.06), respectively. In the dual- and triple-head images, only retrosplenial cortex (bilateral) coefficients of variation met this criterion. The dual-head coefficients of variation were 0.28 (±0.07) and 0.26 (±0.06) for the left and right retrosplenial cortex, respectively. The triple-head coefficients of variation were 0.35 (±0.06) and 0.32 (±0.05) for the left and right retrosplenial cortex, respectively.

TABLE 3
Mean Normalized Counts and Mean Coefficients of Variation Across ROIs for 3 SPECT Templates*

Camera	Measure	Mean	SD	Minimum	Maximum
Single-head	Normalized counts	0.76	0.10	0.57	1.00
	Coefficient of variation	0.18	0.06	0.07	0.32
Dual-head	Normalized counts	0.81	0.07	0.67	1.01
	Coefficient of variation	0.17	0.03	0.11	0.28
Triple-head	Normalized counts	0.83	0.07	0.64	1.00
	Coefficient of variation	0.19	0.04	0.11	0.35

*Excluding white matter and cerebrospinal fluid.

The overall accuracy of the ROIs was further assessed by calculating ratios of gray matter to white matter for each camera. Catafau et al. (*6*) found this ratio to be 1.4:1 using mean occipital rCBF ratios as the index of gray matter. In that study, the values were 1:1 for the single-head camera and 1.3:1 for the dual- and triple-head cameras. The values for the single-head camera were lower than expected, likely because of partial-volume effects.

Hemispheric Asymmetry

Asymmetry was evaluated in 2 ways. First, to determine which regions showed consistent asymmetry across subjects, the mean differences between the 39 bilateral ROIs (including white matter and cerebrospinal fluid) were assessed by paired t tests (Bonferroni adjusted for multiple comparisons, $P < 0.0013$ in all instances, 2-tailed $\alpha = 0.05$). Second, percentage asymmetry values were calculated for the bilateral ROIs to provide a measure of both the magnitude and the direction of asymmetry. This value was calculated using the formula $([R - L]/[R + L]/2) \times 100$, where R = right and L = left. The absolute values were used to determine normative values for the magnitude of hemispheric asymmetry among the ROIs.

Among the 3 cameras, several regions showed consistent statistically significant asymmetry. Of the 39 ROIs, 5 showed asymmetry with all cameras, and an additional 12 were asymmetric with 1 or 2 cameras. Areas identified as asymmetric with all cameras included the cuneus, occipital

TABLE 4
Mean Absolute Asymmetries, Mean Signed Asymmetries, and Proportion of Subjects with Right Asymmetry for Regions Showing Significant Hemispheric Differences

ROI	Single-head	Dual-head	Triple-head
Regions showing asymmetry with all cameras			
Cuneus	**13.20 (5.21); 13.20 (5.21)** **1.00**	**7.31 (3.54); 7.31 (3.54)** **1.00**	**9.94 (5.19); 9.94 (5.19)** **1.00**
Middle frontal gyrus, posterior	**6.00 (3.48); 5.90 (3.67)** **0.93**	**4.63 (3.47); 4.04 (4.18)** **0.83**	**5.05 (2.77); 4.46 (3.70)** **0.85**
Middle temporal gyrus	**6.82 (3.16); 6.71 (3.42)** **0.93**	**5.73 (3.94); 5.35 (4.48)** **0.83**	**6.91 (4.38); 6.31 (5.27)** **0.85**
Occipital cortex	**7.36 (3.00); 7.36 (3.00)** **1.00**	**4.30 (2.41); 4.04 (2.84)** **0.89**	**5.72 (2.62); 5.72 (2.62)** **1.00**
Occipital pole	**12.68 (9.19); 12.56 (9.36)** **0.93**	**5.45 (4.75); 5.10 (5.15)** **0.83**	**7.45 (3.97); 7.09 (4.63)** **0.92**
Regions showing asymmetry with 1 or 2 cameras			
Angular gyrus	**5.55 (3.35); 4.79 (4.44)** **0.87**	**4.98 (3.52); 4.40 (4.26)** **0.94**	2.84 (2.12); 1.76 (3.14) 0.77
Caudate/putamen	3.18 (2.82); 2.60 (3.40) 0.80	**6.09 (3.81); 6.01 (3.95)** **0.94**	**8.15 (3.54); 8.10 (3.67)** **0.92**
Cingulate3	**5.11 (3.62); −4.49 (4.42)** **0.13**	5.61 (3.43); −2.35 (6.27) 0.33	6.10 (5.67); −3.40 (7.74) 0.38
Inferior temporal gyrus	2.52 (2.23); 0.01 (3.43) 0.40	**6.25 (3.55); −6.04 (3.93)** **0.06**	3.09 (2.43); −0.52 (3.99) 0.46
Lingual gyrus	5.69 (4.68); 4.24 (6.11) 0.73	**5.49 (3.91); 4.73 (4.85)** **0.83**	5.32 (4.41); 4.63 (5.19) 0.85
Middle frontal gyrus, anterior	4.19 (3.42); −1.55 (5.28) 0.47	**3.18 (2.29); 2.89 (2.66)** **0.89**	2.87 (2.34); 1.33 (3.53) 0.54
Precuneus	**6.52 (3.62); −6.52 (3.62)** **0.00**	3.40 (2.42); −2.71 (3.22) 0.22	4.34 (2.38); −2.83 (4.17) 0.14
Superior frontal gyrus, posterior	3.88 (2.47); 2.09 (4.20) 0.73	**4.33 (3.09); 3.83 (3.72)** **0.70**	4.25 (3.31); 3.62 (4.04) 0.77
Superior parietal lobe	**6.78 (5.02); 6.46 (5.45)** **0.87**	4.63 (2.76); 3.38 (4.26) 0.83	**5.87 (2.47); 4.93 (4.13)** **0.85**
Supramarginal gyrus	4.56 (3.35); 2.32 (5.27) 0.60	**6.15 (3.85); 5.75 (4.46)** **0.83**	2.95 (2.36); 2.23 (3.10) 0.85
Temporal pole	5.63 (4.37); 4.37 (5.72) 0.73	**4.20 (3.02); 3.71 (3.64)** **0.89**	6.42 (5.62); 4.29 (6.74) 0.77
Thalamus/hypothalamus	**3.94 (3.02); 3.83 (3.17)** **0.93**	3.85 (3.73); 2.46 (4.81) 0.72	4.64 (3.24); 3.81 (4.26) 0.77

First two values are mean (±SD) percentage asymmetries, with mean absolute asymmetry on left and mean signed asymmetry on right. Values for all ROIs are available from authors. Value beneath is proportion of individuals showing right asymmetry.

Bold-faced values are significant by paired *t* test, Bonferonni adjusted for multiple comparisons within camera, with $P = 0.0013$. For a region to show significant right–left differences by this method, right–left asymmetries must be consistent across individuals.

cortex, occipital pole, middle temporal gyrus, and posterior middle frontal gyrus (BA 8/9). These regions showed higher right hemisphere ratios in 83%–100% of healthy volunteers. Table 4 presents the absolute magnitudes of asymmetry and the direction of asymmetry (indicated by the proportion of individuals for whom the right side was greater than the left side) for all regions with significant right–left differences. The mean signed asymmetry values are also provided for comparison with previous PET studies (*23,24*). The mean absolute magnitudes of asymmetry for regions showing mixed asymmetry (and therefore no consistent right–left differences across individuals) ranged from 2.52% to 5.69%, 2.19% to 7.64%, and 2.08% to 8.26% with the single-, dual-, and triple-head cameras, respectively.

Differences in rCBF Ratios Among Cameras

Two sets of comparisons were made among cameras: single-head images were compared with dual-head rCBF ratios for 7 individuals, and dual-head rCBF ratios were compared with triple-head rCBF ratios for 11 individuals. Because the single-head data were already corrected for HMPAO backdiffusion, the dual-head data required correction for backdiffusion before comparison with single-head data. Backdiffusion correction did not alter any results for the dual–triple comparison, so we chose to report the uncorrected values in this instance. For each comparison, individuals were scanned within a few hours on the same day with the 2 cameras after a single injection of HMPAO. For the dual–triple comparison, 5 of the 11 individuals were

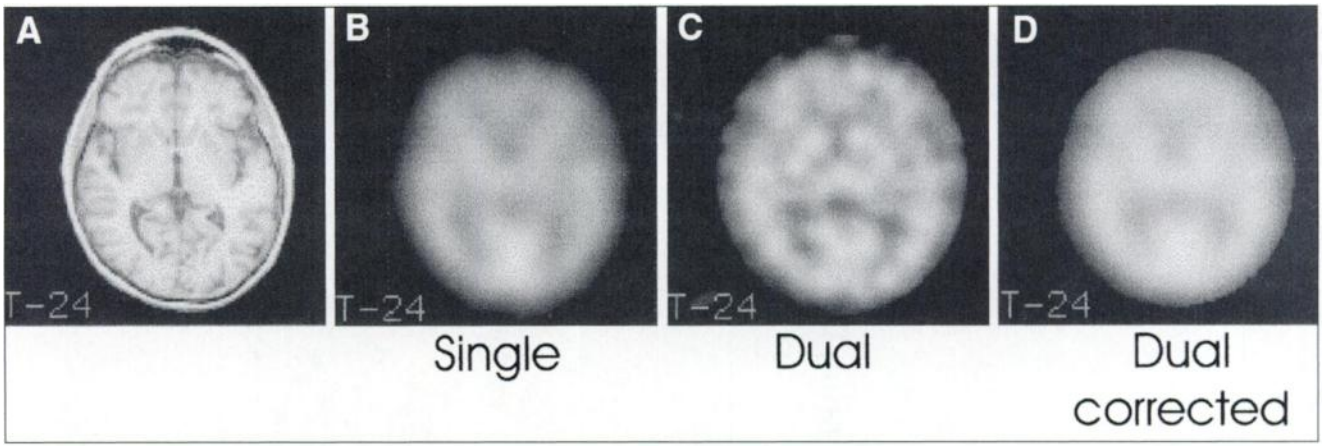

FIGURE 2. Effects on image quality of smoothing dual-head images (C, nonsmoothed, and D, smoothed) to match single-head image (B). Images have been coregistered to baseline MR image (A). Images are from healthy volunteer who served as baseline for templates.

scanned with the dual-head camera first. The time between scans was 40 ±12 min, with a range of 24–60 min. The ratios were compared using paired *t* tests and were Bonferroni adjusted for the 79 ROI comparisons. All reported results are significant at $P < 0.00063$ (2-tailed $\alpha = 0.05$).

No ROI reached statistical significance in the comparison of the rCBF ratios with the dual- and triple-head cameras. The correlation of the mean rCBF ratios across ROIs between these 2 cameras was 0.96 (within-subject correlations ranged from 0.75 to 0.89). The high correlations, combined with the lack of significant differences among cameras, suggest that when images from these 2 cameras are aligned to the appropriate template, the ratios obtained are equivalent. Mean asymmetry values (signed) were evaluated on this subset of healthy volunteers and were also consistent between the 2 cameras ($r = 0.81$).

Striking differences were found between rCBF ratios obtained with the single- and dual-head systems. Initially, we compared the dual- and single-head images directly. Of the 79 ROIs, 43 were significantly different, and the correlation of mean rCBF ratios across ROIs was 0.58. To ensure that these differences were not a function of differences in spatial resolution or spatial filtering between the cameras, we equated the signal between these cameras for statistical analysis. The resolution of the dual-head images was reduced by reconstructing the images using filter parameters similar to those used for the single-head camera. Dual-head images were then visually similar to those produced by the single-head camera (Fig. 2); thus, the reconstructed images were aligned to the single-head template for further analysis. The mean counts per ROI for the filtered dual-head ROIs were adjusted with the equation of Lassen et al. (*13*), using the cerebellar ROI as the reference, and rCBF ratios were calculated. Of the 79 ROIs, 39 were statistically significantly different, although the correlation among cameras increased to 0.93, (within-subject correlations ranged from 0.90 to 0.94). Figure 3 shows this change in correlation for the mean ROI values among cameras. Figure 4 shows data from 2 individuals who underwent single–dual and dual–triple scanning approximately 1 y apart. These scatterplots reveal the magnitude of the discrepancies between the single- and dual-head cameras and the relative lack of discrepancy between the dual- and triple-head cameras.

DISCUSSION

The described technique affords a higher degree of anatomic specificity than do other quantitative, automated or semiautomated, ROI-based approaches currently available. These alternate techniques define the edge of the cortex on individual images, followed by placement of an annular cortical rim (*22,26,27–29*) or a series of annular ROIs to create macrovoxels (*7,30*). In the first technique, the ROIs frequently extend across multiple cortical areas, leaving the user to decide, often arbitrarily, how to designate the anatomic equivalent. In the second technique, an elaborate algorithm was developed to identify the approximate location of each macrovoxel (*7*). In both techniques, ROIs are fit to individual images, and the relation between ROI location and anatomy may not be consistent among subjects.

By aligning the images to a known, standardized space, we eliminated differences caused by variable placement of ROIs by different observers (*31*) and we avoided the anatomic ambiguity inherent in the cortical rim approach. Only 2 sets of linear transforms of the SPECT data are required to obtain the ROI rCBF ratios: a transform into template space followed by a transform into stereotactic space. Although the use of a single healthy volunteer to define the anatomic boundaries may pose problems because of individual differences in regional boundaries, this approach is being successfully applied in other image registration procedures (*32*). In addition, by being expressed in the same space as the SPECT templates, the MR image is somewhat smoothed. This manipulation, combined with the size of the ROIs and the limited spatial resolution of SPECT,

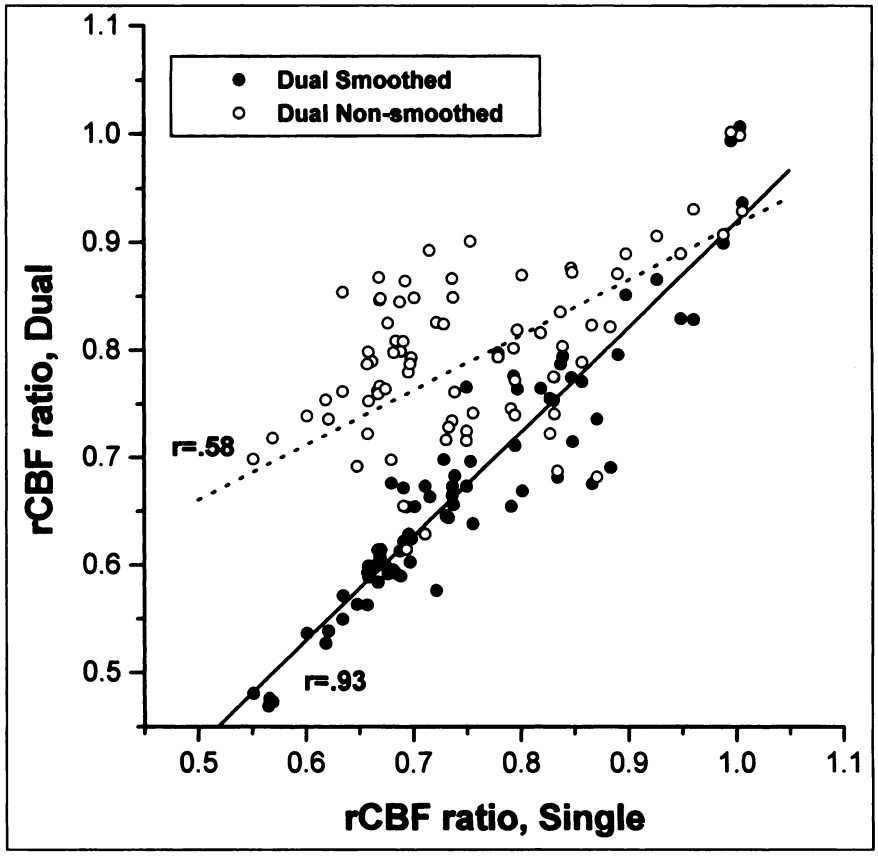

FIGURE 3. Scatterplots of mean ROI rCBF ratios for single-head images with corrected (●) and uncorrected (○) dual-head images. Linear fit is shown in dotted lines for uncorrected and solid lines for corrected rCBF ratios. With smoothing, correlation between cameras increased significantly ($z = 9.678$, $P < 0.001$, 2-tailed). However, single-head rCBF ratios were generally higher than smoothed dual-head ratios, and 39 ROIs were significantly different.

should minimize the impact of individual differences in regional boundaries on the ROI rCBF values. Thus, the approach is intermediate to that of manually placed ROIs on SPECT images coregistered to MR images and the approaches that apply cortical rim ROIs to SPECT data. The degree of overlap in actual anatomic regions across the ROIs is likely to be greater than with the coregistration approach but is less than with the cortical rim approach.

Other investigators have used common spaces to assess changes in brain function with aging (*19*) but have relied on atlases derived from young, healthy volunteers (*33*). The approach of Migneco et al. (*34*) is similar to ours in that it is based on the anatomy of a single individual. Migneco et al. applied the coordinate system of Talairach and Tournoux (*20*), one of the most commonly referenced stereotactic atlases, to SPECT images. A series of 2-dimensional cortical ROIs was generated using short line segments based on the coordinates of Talairach and Tournoux and was applied to lateral cortical projection maps. These projection maps were calculated by averaging flow from cortical regions at the midline and lateral surface, which poses problems for accurate measurements of flow differences in the cortical rim. One additional problem that comes from using the system of Talairach and Tournoux to define ROIs is that its ability to localize cortical boundaries is less precise than its ability to localize subcortical structures (*35*). Our system has an advantage over that of Migneco et al. in that the ROI map uses volumetric rather than 2-dimensional ROIs and bases them on readily identifiable surface landmarks. Thus, although our approach does not allow the high-level anatomic precision seen with MRI SPECT coregistration, generalization across subjects with a reasonable degree of anatomic precision is possible. Because the ROIs are based on an MR image in stereotactic space, generation of equivalent Talairach–Tournoux coordinates for any location within the volume is possible (*35*).

The normative ROI rCBF ratios provide a basis for examining rCBF changes in elderly people. The joint use of ROI rCBF ratios and ROI coefficients of variation may be useful for localizing potential regions of atrophy or lesions in cases of stroke. Alaamer et al. (*36*) showed that within a volume, activity variations of as much as 100% had minimal impact (3%) on the measure of activity in the volume, although the volume estimate was affected by activity differences. This finding indicates that ROIs containing low flow because of atrophy are likely to be missed in the inspection of rCBF ratios. However, the coefficient of variation provides an index of ROI variability and increases substantively when an ROI contains voxels with extremely low counts. Our normative values are consistent with PET ROI techniques (*37*) and with the SPECT phantom study of Alaamer et al. (They did not find a linear relation across levels of variation in activity, but they were simultaneously estimating volume, which did change. The fixed-ROI approach is likely to be more sensitive to the effects of ROI nonuniformity.) We are currently assessing whether ROIs

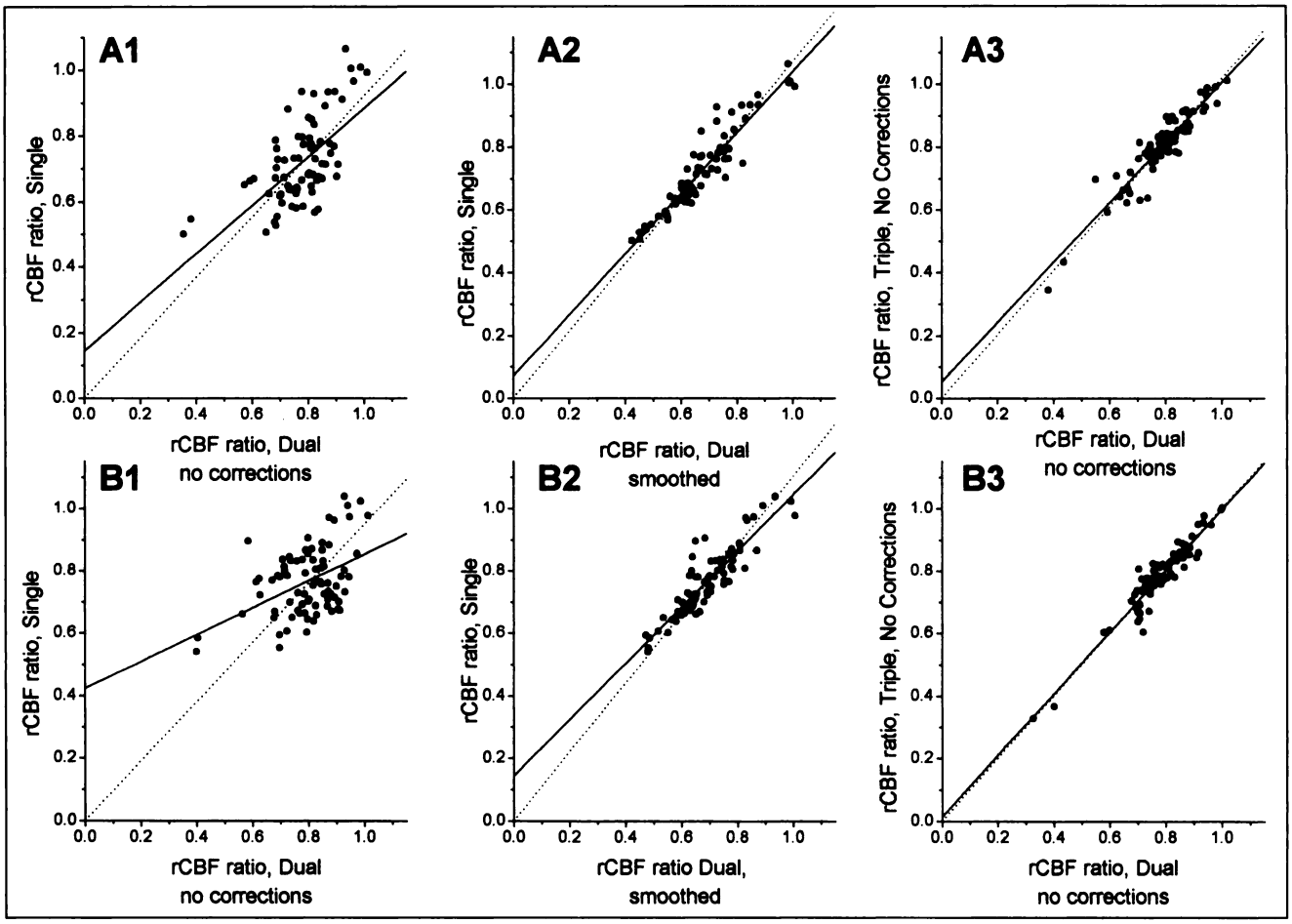

FIGURE 4. Comparisons of rCBF ratios from single–dual and dual–triple cameras for 2 healthy volunteers with data from all 3 cameras. Ideal fit through data is shown as dotted lines, and actual fit is shown as solid line. Top row is healthy volunteer A (base image for templates), bottom row is healthy volunteer B. A1 and B1 show relationship between single-head image and nonsmoothed dual-head image. A2 and B2 show relationship between single-head image and smoothed dual-head image. A3 and B3 show relationship between triple-head and nonsmoothed dual-head image. Fits for smoothed dual–single plots are better than those for nonsmoothed dual–single plots and are similar to those for dual–triple plots, reflecting pattern shown across individuals in Figure 3. For both individuals, outlier points are from cerebrospinal fluid ROIs.

with coefficients of variation greater than expected on the basis of control values, with or without concomitant decreases in normalized counts, reflect atrophy or low flow caused by a lesion.

Many ROI approaches, both cortical rim and manually placed (*6,38*), have used bilaterally symmetric ROIs, thus potentially masking inherent hemispheric asymmetries in ROI size or location. In our study, like other SPECT studies, consistent asymmetries were found in posterior and temporal regions with all 3 cameras. Significant asymmetries (right greater than left) were recently noted in parietal, occipital, and temporal ROIs in a SPECT study comparing healthy young individuals with healthy elderly individuals (*6*). Hemispheric perfusion measured by SPECT has also been shown to be higher in the right than the left hemisphere, using both cerebellar and whole-slice reference regions (*8*). SPECT asymmetries contrast with those found in PET studies of resting glucose metabolism. Typically, in healthy elderly individuals, PET shows smaller right–left differences (1%–2%) than the differences we found. In some regions, asymmetries were in the opposite direction as well. Because the PET values were averages of signed asymmetries (*24,25*), the discrepancies between the SPECT and PET asymmetries may reflect higher rates of mixed asymmetries in glucose uptake. We could identify as significant only regions where the direction of asymmetry was consistent across individuals. This relationship was not directly assessed in the PET studies. Typically, 12%–13% is considered the upper limit for normal asymmetry in both qualitative (*39*) and semiquantitative (*40*) rCBF studies. Therefore, the magnitude differences between our study and PET studies may reflect biologic variability as well as methodologic differences.

More important than the consistency of asymmetry direction are the normative values for absolute hemispheric asymmetry that our technique provides, because these can be useful in tracking functional impairment in dementia. Regional asymmetries were larger in mildly demented

patients with Alzheimer's disease than in healthy volunteers, initially increasing in magnitude and then later evolving to equivalent bilateral hypoperfusion (*24*). Additionally, a recent study directly examined rCBF with ^{133}Xe in a group of patients with age-related cognitive decline and found that small asymmetries were important (*41*). In a subgroup of patients, who became demented within 1–3 years, parietotemporal asymmetries of 9% (our calculations) were present at the initial examination. This asymmetry was statistically different from that in healthy volunteers, whose values were approximately 4%. Small changes in asymmetry magnitude thus may have clinical significance, indicating that initial (normal) asymmetry magnitude, irrespective of direction, must be considered when evaluating the significance of asymmetries present in patients with diseases such as Alzheimer's.

To our knowledge, this report is the first to explicitly address the issue of whether semiquantitative rCBF data obtained with different cameras produce similar values. Although the sample sizes available for testing this issue were small, we suggest that the 2 systems with higher resolutions provide similar rCBF measures. The results indicate that if images are aligned to the appropriate template (dual to dual, triple to triple), the calculated rCBF ratios can be combined for statistical analysis. However, our analysis also suggests it is not possible to combine rCBF ratios from single- and dual-head systems. Discrepancies in ratios were not caused simply by smoothing differences between cameras, because the number of significantly different ROIs did not change appreciably when the dual-head images were smoothed to the level of the single-head images. Thus, on one hand, caution is suggested in any direct comparisons of rCBF ratios between these low- and high-resolution cameras. On the other hand, the smoothed dual-head images have a more consistent relationship with the values obtained from the single-head images, as the significant correlation increase across ROIs shows (from 0.58 to 0.93). Additionally, relations among ROIs appear to be similar across the 2 cameras, because the measures of right–left asymmetry did not differ statistically and correlated strongly (r = 0.89). Thus, if one is willing to forgo resolution by smoothing dual-head images, one may possibly, in a statistical analysis, combine measures from these cameras on the basis of interregional relations.

CONCLUSION

Three HMPAO SPECT templates—for single-, dual- and triple-head γ cameras—have been developed using elderly healthy volunteers, providing an age-appropriate common space to represent SPECT images. The ROI map was created in an MR image–based anatomic space and provides a way to obtain normative values for rCBF ratios, hemispheric asymmetries, and rCBF variability in elderly individuals. Site-specific norms can easily be created, and with the incorporation of additional images, values based on demographic variables such as sex or age groupings (young–old versus old–old) can also be generated. A major benefit of this approach is quick acquisition of ROI values (10 min per brain) with minimal operator intervention. Analysis of values from the 3 cameras showed that data from single-head cameras cannot easily be combined with data from high-resolution cameras but that rCBF values from dual- and triple-head cameras can be treated as equivalent. The values obtained from these templates provide a foundation for detecting disease-related rCBF alterations in elderly individuals.

APPENDIX

Preparation of Base MR Image

The base T1-weighted MR image (256 × 256 × 124 voxels; voxel size, 0.859 × 0.859 × 1.20 mm) was manually oriented into stereotactic space using ANALYZE AVW, version 1.1. The final image size was 256 × 256 × 145 voxels, at 0.859 mm^3/voxel.

The skull and meninges were eroded using iMIPS.

The eroded image was resliced using AIR, version 3.07, into a 128 × 128 × 50 voxel space, with anisotropic voxels measuring 1.72 × 1.72 × 2.66 mm each.

Preparation of Templates

All SPECT images in the template were aligned to the base image using the 12-parameter affine model in AIR, version 3.07. (Syntax: alignlinear <BaseSPECT> <SubjectSPECT> <ResliceFile.air> -m 12 -x 3 -c 0.005 -t1 80 -t2 80 -z -v.)

Common space for all images was defined. (Syntax: definecommon_air <input prefix> <input suffix> <output prefix> <output suffix> y <subjID>.)

Coregistered image files were created using reslice parameters from definecommon_air step. (Syntax: reslice <CommonOutput.air> <CommonOutput> -k.)

Coregistered images were averaged, and any voxels with 0 values were treated as missing data and not included in the average. (Syntax: softmean <TemplateName> y null <list of image files>.)

Alignment of Templates to MR Image

BaseSPECT_to_BaseMRI: For each camera, the base SPECT image was aligned to the resliced MR image using the 6-parameter rigid-body model. (Syntax: alignlinear <BaseMRI> <BaseSPECT> <ResliceFile.air> -m 6 -t1 10 -t2 80 -r 100 -z -v.)

BaseSPECT_to_Template: The base SPECT images were aligned to the appropriate template to provide parameters for reslicing the base images into template space. (Syntax: alignlinear <Template> <BaseSPECT> <ResliceFile.air> -m 12 -x 3 -c 0.005 -t1 80 -t2 80 -z -v. These files are not needed after inverting [next step].)

Template_to_BaseSPECT: Inverse of BaseSPECT_to_Template, this function gives the parameters for reslicing the template to the base SPECT image. (Syntax: invert_air <BaseSPECT_to_Template> <Template_to_BaseSPECT>.)

Template_to_MRI: Created with combine_air. (Syntax: combine_air <Template_to_BaseMRI.air> y <BaseSPECT-_to_BaseMRI.air> <Template_to_BaseSPECT.air>. The order is important; see AIR documentation for further information.)

The template was resliced into MR image space in 1 step (no intermediate images were created). (Syntax: reslice <Template_to_BaseMRI.air> <Template_to_BaseMR> -k. This was used only for examining the accuracy of the ROI map.)

Alignment of New SPECT Images to Template and Baseline MR Images

The basic syntax used to align patient SPECT images to the appropriate template and to reslice them into MR image space for applying the ROI template appears below.

alignlinear <TEMPLATE> <PatientSPECT> <AIR-file.air> -m 12 -x 3 -r 100 -c 0.005 -t1 80 -t2 80 -z -v> <AIRfile.out>.

combine_air <PatientSPECT_to_BaseMRI.air> y <Base SPECT_to_BaseMRI.air> <Template_to_BaseSPECT.air> <PatientSPECT_to_Template.air>.

reslice <PatientSPECT_to_BaseMRI.air> <PatientSPECT _to_BaseMRI> -k.

ACKNOWLEDGMENTS

This study was supported by grants from the Heart and Stroke Foundation of Ontario, the Ontario Mental Health Foundation, and the Medical Research Council of Canada; an Acenburg fellowship from the Rotman Research Institute; and an MD/PhD studentship from the Medical Research Council of Canada. The authors thank Kira Barbour for recruiting healthy volunteers, the nuclear medicine technical staff for acquiring images, and Guang Thang and Aviv S. Gladman for programming. The templates and detailed descriptions of the normal values can be obtained through anonymous file transfer by contacting nlobaugh@rotman-baycrest.on.ca.

REFERENCES

1. Holman BL, Zimmerman RE, Johnson KA, et al. Computer-assisted superimposition of magnetic resonance and high-resolution technetium-99m-HMPAO and thallium-201 SPECT images of the brain. *J Nucl Med.* 1991;32:1478–1484.
2. Harris GJ, Pearlson GD. MRI-guided region of interest placement on emission computed tomograms. *Psychiatr Res.* 1993;50:57–63.
3. Julin P, Lindqvist J, Svensson L, Slomka P, Wahlund LO. MRI-guided SPECT measurements of medial temporal lobe blood flow in Alzheimer's disease. *J Nucl Med.* 1997;38:914–919.
4. Stollberger R, Fazekas F, Payer F, Flooh E. Morphology-oriented analysis of cerebral SPET using matched magnetic resonance images. *Nucl Med Commun.* 1995;16:265–272.
5. Fox PT, Mintun MA, Reiman EM, Raichle ME. Enhanced detection of focal brain responses using intersubject averaging and change-distribution analysis of subtracted PET images. *J Cereb Blood Flow Metab.* 1988;8:642–653.
6. Catafau AM, Lomena FJ, Pavia J, et al. Regional cerebral blood flow pattern in normal young and aged volunteers: a ^{99m}Tc-HMPAO SPET study. *Eur J Nucl Med.* 1996;23:1329–1337.
7. Jones K, Johnson KA, Becker A, Spiers PA, Albert MS, Holman BL. Use of singular value decomposition to characterize age and gender differences in SPECT cerebral perfusion. *J Nucl Med.* 1997;39:965–973.
8. Krausz Y, Bonne O, Gorfine M, Karger H, Lerer B, Chisin R. Age-related changes in brain perfusion of normal subjects detected by ^{99m}Tc-HMPAO SPECT. *Neuroradiology.* 1998;40:428–434.
9. Mozley PD, Sadek AM, Alavi A, et al. Effects of aging on the cerebral distribution of technetium-99m hexamethylpropylene amine oxime in healthy humans. *Eur J Nucl Med.* 1997;24:754–761.
10. Mahmood S, Buscombe JR, Kouris K, et al. Clinical experience with a multidetector SPET system (Toshiba GCA-9300A). *Nucl Med Commun.* 1994;15: 643–652.
11. Kouris K, Jarritt PH, Costa DC, Ell PJ. Physical assessment of the GE/CGR Neurocam and comparison with a single rotating gamma-camera. *Eur J Nucl Med.* 1992;19:236–242.
12. Fahey FH, Harkness BA, Keyes JW Jr, Madsen MT, Battisti C, Zito V. Sensitivity, resolution and image quality with a multi-head SPECT camera. *J Nucl Med.* 1992;33:1859–1863.
13. Lassen NA, Anderson AR, Friberg L, Paulson OB. The retention of [^{99m}Tc]-d,l-HM-PAO in the human brain after intracarotid bolus injection: a kinetic analysis. *J Cereb Blood Flow Metab.* 1988;8(suppl):S13–S22.
14. Stapleton SJ, Caldwell CB, Ehrlich LE, Leonhardt CL, Black SE, Yaffe MJ. Effects of non-linear flow and spatial orientation on technetium-99m hexamethyl-propylene amine oxime single-photon emission tomography. *Eur J Nucl Med.* 1995;22:1009–1016.
15. Chang LT. A method for attenuation correction in radionuclide computed tomography. *IEEE Trans Nucl Sci.* 1978;NS-26:638–643.
16. Loutfi I, Singh A. Comparison of quantitative methods for brain single photon emission computed tomography analysis in head trauma and stroke. *Invest Radiol.* 1995;30:588–594.
17. Woods RP, Grafton ST, Holmes CJ, Cherry SR, Mazziotta JC. Automated image registration: part 1. General methods and intrasubject, intramodality validation. *J Comput Assist Tomogr.* 1998;22:139–152.
18. Woods RP, Grafton ST, Watson JD, Sicotte NL, Mazziotta JC. Automated image registration: part 2. Intersubject validation of linear and nonlinear models. *J Comput Assist Tomogr.* 1998;22:153–165.
19. Imran MB, Kawashima R, Sato K, et al. Mean regional cerebral blood flow images of normal subjects using technetium-99m-HMPAO by automated image registration. *J Nucl Med.* 1998;39:203–207.
20. Talairach J, Tournoux P. *Co-Planar Stereotaxic Atlas of the Human Brain.* New York, NY: Thieme Medical Publishers; 1988.
21. Damasio H. *Human Brain Anatomy in Computerized Images.* New York, NY: Oxford; 1995.
22. Karbe H, Kertesz A, Davis J, Kemp BJ, Prato FS, Nicholson RL. Quantification of functional deficit in Alzheimer's disease using a computer-assisted mapping program for ^{99m}Tc-HMPAO SPECT. *Neuroradiology.* 1994;36:1–6.
23. Talbot PR, Lloyd JJ, Snowden JS, Neary D, Testa HJ. Choice of reference region in the quantification of single-photon emission tomography in primary degenerative dementia. *Eur J Nucl Med.* 1994;21:503–508.
24. Haxby JV, Grady CL, Koss E, et al. Longitudinal study of cerebral metabolic asymmetries and associated neuropsychological patterns in early dementia of the Alzheimer type. *Arch Neurol.* 1990;47:753–760.
25. Murphy DG, DeCarli C, McIntosh AR, et al. Sex differences in human brain morphometry and metabolism: an in vivo quantitative magnetic resonance imaging and positron emission tomography study on the effect of aging. *Arch Gen Psychiatry.* 1996;53:585–594.
26. Liu HG, Mountz JM, Inampudi C, San Pedro EC, Deutsch G. A semiquantitative cortical circumferential normalization method for clinical evaluation of rCBF brain SPECT. *Clin Nucl Med.* 1997;22:596–604.
27. Ichise M, Crisp S, Ganguli N, Tsai S, Gray BG. A method of 2-dimensional mapping of cortical perfusion by cylindrical transformation of HMPAO SPET data. *Nucl Med Commun.* 1995;16:386–394.
28. Buck BH, Black SE, Behrmann M, Caldwell C, Bronskill MJ. Spatial- and object-based attentional deficits in Alzheimer's disease: relationship to HMPAO-SPECT measures of parietal perfusion. *Brain.* 1997;120:1229–1244.
29. Leibovitch FS, Black SE, Caldwell CB, Ebert PL, Ehrlich LE, Szalai JP. Brain-behavior correlations in hemispatial neglect using CT and SPECT: the Sunnybrook Stroke Study. *Neurology.* 1998;50:901–908.
30. Johnson KA, Kijewski MF, Becker JA, Garada B, Satlin A, Holman BL. Quantitative brain SPECT in Alzheimer's disease and normal aging. *J Nucl Med.* 1993;34:2044–2048.
31. Claus JJ, Dubois EA, Booij J, et al. Demonstration of a reduction in muscarinic receptor binding in early Alzheimer's disease using iodine-123 dexetimide single-photon emission tomography. *Eur J Nucl Med.* 1997;24:602–608.
32. Kabani N, MacDonald JD, Holmes CJ, Evans AC. 3D anatomical atlas of the human brain [abstract]. *Neuroimage.* 1998;7(suppl 4, pt 2):S717.
33. Roland PE, Graufelds CJ, Wåhlin L, et al. Human brain atlas: for high-resolution functional and anatomical mapping. *Human Brain Mapp.* 1994;1:173–184.

34. Migneco O, Darcourt J, Benoliel J, et al. Computerized localization of brain structures in single photon emission computed tomography using a proportional anatomical stereotactic atlas. *Comput Med Imaging Graph.* 1994;18:413–422.
35. Woods RP. Correlation of brain structure and function. In: Toga AW, Mazziotta JC, eds. *Brain Mapping: The Methods.* San Diego, CA: Academic Press; 1996:313–341.
36. Alaamer AS, Fleming JS, Perring S. Evaluation of the factors affecting the accuracy and precision of a technique for quantification of volume and activity in SPECT. *Nucl Med Commun.* 1994;15:758–771.
37. Camargo EE, Szabo Z, Links JM, Sostre S, Dannals RF, Wagner HN Jr. The influence of biological and technical factors on the variability of global and regional brain metabolism of 2-[^{18}F]fluoro-2-deoxy-D-glucose. *J Cereb Blood Flow Metab.* 1992;12:281–290.
38. Vlasenko A, Petit-Taboue MC, Bouvard G, Morello R, Derlon JM. Comparative quantitation of cerebral blood volume: SPECT versus PET. *J Nucl Med.* 1997;38:919–924.
39. Pickut BA, Saerens J, Marien P, et al. Discriminative use of SPECT in frontal lobe-type dementia versus (senile) dementia of the Alzheimer's type. *J Nucl Med.* 1997;38:929–934.
40. Podreka I, Suess E, Goldenberg G, et al. Initial experience with technetium-99m HM-PAO brain SPECT. *J Nucl Med.* 1987;28:1657–1666.
41. Celsis P, Agniel A, Cardebat D, Demonet JF, Ousset PJ, Puel M. Age related cognitive decline: a clinical entity? A longitudinal study of cerebral blood flow and memory performance. *J Neurol Neurosurg Psychiatry.* 1997;62:601–608.